Analysis of Sliding Contact of Armature Inside the Vertical Curved Rails in Electromagnetic Railgun

Yunlong Che, Weiqun Yuan, Wu Yuan, Zhizeng Wang, Wei Hao, Ying Zhao, and Ping Yan

Abstract— In previous studies, the armature–rail sliding contact interface is usually considered to be an ideal slide in which both rails are parallel and symmetric. However, due to the influence of structural deformation of the barrel affected by boundary constraints and the manufacturing errors of rails and armature, it often leads to a variety of nonideal armature–rail matching such as space curved or twisted rails, offset or deflected armature, and so on. This article focuses on the common vertical curved rail in electromagnetic railgun. By introducing centrifugal force effects and coupling electromagnetic force, the armature–rail contact pressure is analyzed theoretically. According to the 3-D finite-element simulation results, the effect of centrifugal force on sliding contact pressure should not be ignored. The effects of different curved radii, velocities, and densities of armature on the contact pressure are compared and analyzed. The influence law on the contact pressure is obtained, which provides a theoretical basis for the design of the railgun.

Index Terms— Armature, centrifugal force, contact pressure, curved, rail, railgun.

I. INTRODUCTION

THE railgun is an equipment that converts electric energy into instantaneous kinetic energy in a short time. It has advantages over traditional methods in controllability and life-span cost. Moreover, it has great strategic significance in both military and civilian fields. The ideal armature–rail matching should be that the armature center coincides with the caliber center which is assembled from the metal electrode and the insulating component. The armature moves in a straight line at high speed along the center line of the caliber driven by the electromagnetic force generated by the large pulse current. A stable and low armature contact resistance (generally microohms) is expected during the launching process to maintain good armature sliding electrical contact performance at super high speed. But, due to the influence of structural deformation of the barrel affected by boundary constraints

and the manufacturing errors of rails and armature, it usually leads to a variety of nonideal armature–rail matching such as space curved or twisted rails, offset or deflected armature, and so on.

In previous studies, the armature–rail sliding contact interface is usually considered to be an ideal slide in which both rails are parallel and symmetric. In 2013, Huazhong University proposed a nonequal-cross-section cantilever model for C-type armature, and the equation of armature deformation is established and verified experimentally [1]. In 2015, the 3-D model of the armature–rail contact pressure was established, the typical contour diagram of the nonuniform contact pressure distribution was obtained, and uniformity coefficients affecting the contact pressure distribution were proposed to evaluate the contact performance [2]. At present, it is not common to consider the axial stiffness of the barrel in the available data. In 2001, the University of Texas proposed the evaluation of the axial stiffness of the barrel to restrain drooping and torsion [3]. In 2005, the University of Texas proposed a lightweight and high-stiffness emitter barrel structure, which adopts multiple nesting of thin-walled cylindrical parts to achieve pretightening force while ensuring high axial stiffness of the barrel [4]. In literature [5], [6], [7], [8], [9], [10], [11], the armature–rail sliding contact, axial stiffness, and dynamic response of the barrel were studied, respectively, and the evaluation and improvement methods were obtained, but the problem and action mechanism of the droop caused by the lack of axial stiffness of the barrel are not analyzed.

An external cantilever often supports the barrel in the service environment. The vertical gravity curving and deflection at the end of the barrel are unavoidable under the action of gravity. In the design of the barrel, researchers have adopted measures such as a nonuniform section taper design to improve the axial curving stiffness. The curving degree can only be reduced by the constraints of the external suspension support, but cannot be completely eliminated. When the armature moves along two vertically curved rails, the inertia caused by its own mass forces it to continue to move in the tangential direction of the rails, resulting in radial centrifugal force and reaction support between the armature and the rail. In addition, the other part of the armature–rail contact pressure is generated by electromagnetic force to ensure the sliding electrical contact performance in high-speed motion. In the transient centrifugal motion, the complex coupling of both leads to the asymmetric distribution of the armature–rail contact pressure, which is generally composed of over contact and loss contact. From the

Fig. 1. Sample of the figure caption.

Fig. 2. Schematic diagram of the force analysis of the curved rail and armature under the launch transient.
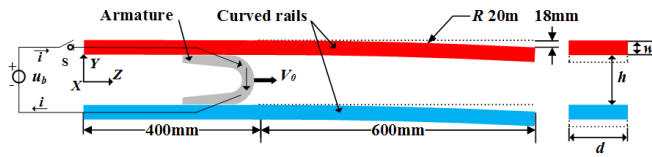
perspective of over contact, if the critical overpressure of contact pressure is reached, permanent plastic deformation will occur, such as rail planning and armature failure. On the other hand, compared with the over contact, loss pressure may cause the liquid metal layer on the contact area to separate from the armature, resulting in the deterioration of sliding electrical contact, transition, ablation, and other phenomena. This article considered the vertical curved barrel structure in the railgun. The armature–rail contact pressure is analyzed theoretically by introducing centrifugal force effects and coupling electromagnetic force. The influence of curved radii, velocities, and densities of armature on contact pressure is analyzed through a 3-D simulation example, which provides a theoretical basis for the design of electromagnetic launch devices.

II. ANALYSIS OF FORCE ON CURVED RAIL AND ARMATURE DURING LAUNCH

The simplified launcher consists of two rails of finite length with the same curvature and an armature that is placed between the two rails. With the center position of the end of the two rails as the origin, the length direction as the X-axis, the vertical direction of the rail as the Y-axis, and the direction perpendicular to the XOY-plane as the Z-axis, the established coordinate system is established. During the firing process, the armature moves at high speed in the direction of the X-axis line under the action of the initial velocity.

A. Geometric Model

In the model, the rail is made of copper alloy, and the armature is made of aluminum alloy, which adopts an isotropic elastic material model. Table I shows the constitutive parameters of rail and armature materials. Table II shows the geometric parameters of caliber in the simulation Settings. As shown in Fig. 1, H represents the distance between the two contact surfaces, W represents the thickness of the rail, and D represents the width of the interaction between the rail and the armature. The curved rail is divided into two sections along the length direction in the simulation model. The front section is an ideal long straight rail with a length of 400 mm, and the back section is a nonideal curved rail with a length of 600 mm, a curving radius of 20 m, and a port deflection of about 18 mm. The armature is of C-type construction with a total length of 23 mm.

B. Boundary Conditions

Considering the high velocity of the armature passing through the curved rails, the boundary condition is simplified in that all displacements and angles of the rail support surfaces
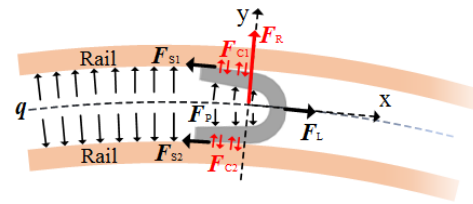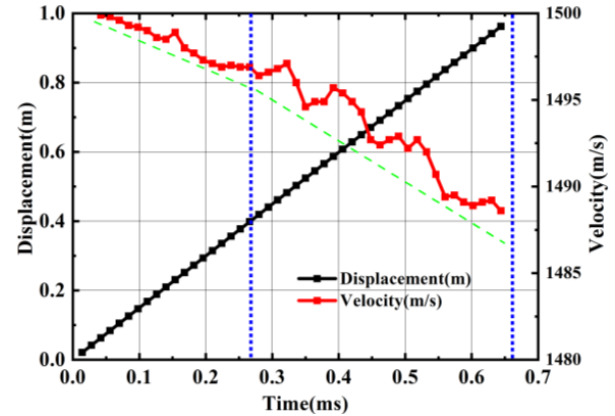

Fig. 3. View of armature velocity and displacement over time.

TABLE I
MATERIAL CONSTITUTIVE PARAMETERS

Material	Material	E (GPa)	v	ρ (kg/m³)
Rail	Copper alloy	128	0.35	8900
Armature	Aluminum alloy	70	0.33	2750

TABLE II
GEOMETRIC PARAMETERS OF CALIBER

Geometric parameters	H (mm)	W (mm)	D (mm)
value	16	10	12

are fixed, and the armature of displacement perpendicular to the contact surface is constrained.

In the simulation model, the armature expands and presses against the rail under the electromagnetic force, and the armature–rail friction contact is established with the static friction coefficient of 0.15 and the sliding friction coefficient of 0.1 by using the generalized Lagrange contact algorithm.

C. Load Conditions

Generally, the rail length is much larger than the curved deflection in the launcher, so this article assumes that the curved rail is continuous and uniform.

Define the position of the tangent and armature center of mass over the curved bore as the X-direction and the vertical rail surface as the Y-direction in Fig. 2. F_R is the centrifugal force on the armature, F_L is the electromagnetic force on the armature, F_{c1} and F_{c2} are the armature–rail contact forces on the upper and lower, F_{s1} and F_{s2} are the frictional forces on the upper and lower tail of the armature, and q is the electromagnetic repulsion set between the two rails.

The electromagnetic force F_L is derived from the integration of the Biot–Savart law [12]

$$F_L = \frac{1}{2} L' I^2 \tag{1}$$

where L' is the inductance gradient and I is the current.

The armature–rail contact force of the long straight section under the action of electromagnetic force F_C can be expressed as follows [13]:

$$F_C = \frac{1}{2} \beta L' I^2 \cos\theta + F_P(\varepsilon) \tag{2}$$

where F_P is the pressure caused by the armature–rail interference fit, which is related to the amount of interference ε, β is the coefficient of the squeezing force on the rail (value: 0.42), which is related to the component of the electromagnetic force on the armature tail vertical to the rail direction, and θ is the angle of armature tail.

In order to simplify the simulation calculation, this article focuses on analyzing the influence of the curved rail factor under the action of constant current, ignoring the role of rising and falling current. The initial loading speed of the armature is 1500 m/s, and the simulation time is 0.07 ms to ensure that the armature moves out of the bore. From the circuit simulation, the current is calculated to be about 120 kA, and the inductance gradient is 0.36 μH/m. The contact pressure of about 1200 N is calculated equivalently from (3). Finally, the initial equivalent contact pressure of the electromagnetic force and interference fit is calculated to be about 5 MPa by dividing the contact force by the inner surface area of the armature.

According to Newton's law of motion in the rotating reference system (noninertial reference system), the formula of normal centrifugal force F_R received by the accelerated object in the high-speed motion along the vertical curved bore can be expressed as follows:

$$F_R = \frac{m\dot{x}^2}{R(x, t)} \tag{3}$$

where $R\ (x,\ t)$ represents the curve radius of the rail at the x-coordinate at time t; m is the mass of the armature, and the direction of centrifugal force deviates from the center of the curve radius.

Under the action of transient centrifugal force, the armature is subjected to the Y-component of the centrifugal force and the support force of the upper orbit on the overcontact side to restrain the armature from excessive Y-displacement. Therefore, the upper and lower contact pressures F_{c1} and F_{c2} are asymmetric, and the frictional forces F_{s1} and F_{s2} on the upper and lower arms of the armature can be expressed as follows:

$$F_{S1\&2} = \mu F_{C1\&2} \tag{4}$$

where μ is the sliding friction coefficient.

The armature fluctuation of sliding friction is not symmetrical from formula (4). This difference in the vector will make the armature deflect toward the overpressure side and prevent the armature from deflecting along the curved rail. There is a slight angle difference between the motion direction of the armature and the symmetry axis of the armature structure.

It may cause the contact area on the overpressure side to move forward and the loss side to move backward, accompanied by complex structural deformation. To sum up, the finite-element method is used in this article. The contact force and deformation are obtained by solving the node displacement load equation with the finite-element method in solid mechanics

$$\boldsymbol{K}\boldsymbol{d} = \boldsymbol{f} + \boldsymbol{r} \tag{5}$$

where $\boldsymbol{K}$ is the stiffness matrix, $\boldsymbol{d}$ is the stiffness matrix, and $\boldsymbol{f}$ and $\boldsymbol{r}$ are the load and reaction vectors, respectively.

III. ANALYSIS OF SIMULATION

A. Simulation Method

In this article, the transient and nonlinear simulation and analysis of the armature–rail contact process are carried out by using the dynamic display module of the ANSYS workbench. The dynamic control equation based on the nonlinear finite-element method can be expressed as follows [14]:

$$\boldsymbol{M}\ddot{\boldsymbol{x}} + \boldsymbol{C}\dot{\boldsymbol{x}} + \boldsymbol{K}\boldsymbol{x} = \boldsymbol{F}(t) \tag{6}$$

where $\boldsymbol{M}$ represents the mass matrix; $\boldsymbol{C}$ represents the damping matrix; $\boldsymbol{K}$ represents the stiffness matrix; $\boldsymbol{F}$ is the external force matrix; $\ddot{\boldsymbol{x}}$, $\dot{\boldsymbol{x}}$, and $\boldsymbol{x}$ are acceleration, velocity, and displacement matrices, respectively; and $\boldsymbol{t}$ is the time variable. In continuous motion along curved rails, the motion equations of the armature are divided into many differential equations of discrete models, so that the exact solution of the differential equation satisfies the above constraints and loads. The central difference numerical method is used to integrate the display time of formula (6), to solve the stress and strain of the armature in the process of moving in the curved rails.

B. Simulation Results and Analysis

The relationship curve of the armature velocity and displacement with time at the whole launching moment of the simulation results in Fig. 3. The armature moves to the end of the long straight section, enters the bending section at 0.266 ms, and is discharged at 0.658 ms. In the long straight section, the armature can be considered to make uniform deceleration movement under the action of sliding friction. In the curved section, the armature still keeps uniform deceleration motion, but the velocity begins to produce periodic fluctuation under the influence of centrifugal force, and the velocity drop is greater than in that long straight section.

As shown in Fig. 4(a), at 0.126 ms, in the long straight section, the maximum stress distribution and amplitude are similar, which are 5.4 and 6.4 MPa for upper and lower rails, which are 12.03 and 9.65 MPa for upper and lower armature tails produced by an equivalent electromagnetic pressure of 5 MPa, respectively.

As shown in Fig. 4(b), at 0.322 ms, at the beginning of the curving section, the armature–rail contact pressure on both sides is unbalanced under the influence of centrifugal force. The maximum stress of the upper is 10.6 MPa of the rail and 42.14 MPa of the armature, which is significantly greater than that of the lower rail (6.2 MPa) and armature (17.18 MPa)
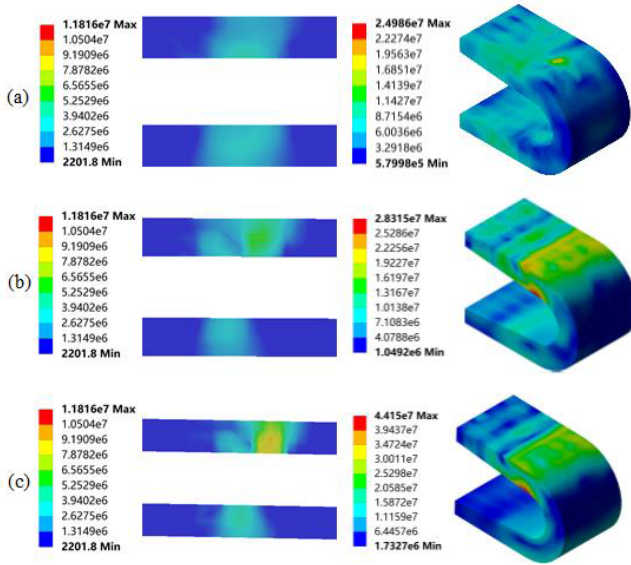
Fig. 4. v-m stress diagram of rails under the impact of the armature and curved rails at different times. (a) At 0.126 ms. (b) At 0.322 ms. (c) At 0.504 ms.

because the curving direction of the rail determines that the centrifugal force of the armature is pressed to the upper rail. Compared with the initial value, the maximum stress of the upper armature and rail increases by 250.3% and 96.3%, and the lower side increases by 79.7% and decreases by 3.1%.

As shown in Fig. 4(c), at 0.504 ms, in the curved section, the maximum stress of both increased significantly and reached the maximum value. The upper armature and rail stress (59.47 and 17.1 MPa) were still greater than that of the lower side (28.08 and 7.9 MPa). Compared with the initial value, the upper sides increase by 394.3% and 216.7%, and the lower side increased by 193.7% and 23.4%. Based on the above analysis, it can be concluded that the influence of centrifugal force on sliding armature–rail contact pressure cannot be ignored when the armature moves at high velocity between two curved rails.

It can be seen that a small range of high-stress regions is formed at the armature–rail contact part and the stress distribution in other noncontact regions is relatively uniform when the armature moves at high velocity between two sections.

IV. Influence Analysis of Armature–Rail Sliding Contact Parameters

In order to further study the sliding contact of curved rail, a multiparameter quantitative analysis was carried out based on the previous analysis results. According to (3), the centrifugal force is mainly affected by the armature speed, mass parameters, and curve radius. This article analyzes the influence rule of the armature–rail contact pressure of the above three parameters. The parameter variables and the analysis table of single parameter variables are shown in Table III (the characteristic values of parameter changes are given in parentheses). The calculation results are shown in Figs. 5–7.

Fig. 5(a) shows that as the curve radius decreases at the initial armature velocity of 1500 m/s, the effect of centrifugal force increases, leading to an obvious periodic velocity

TABLE III
RANGE OF EIGENVALUES OF IMPACT PARAMETERS

Parameters	R (m)	V (m/s)	ρ (kg/m^3)
1	[0 10 20 30]	1500	2700
2	20	[1500 2000 2500]	2700
3	20	1500	[2700 5000 9000]

fluctuation and a larger fluctuation range and velocity drop in the curved section. The outlet velocities are 1490.7, 1489.6, 1489.2, and 1484.7 m/s of four different curve radii in descending order. It can be concluded that with the decrease of curve radius, the armature–rail sliding friction increases, which leads to the increase in energy loss and the decrease of armature outlet velocity. Fig. 5(b) shows that as the armature moves forward to the curved section, the same periodic fluctuation of the armature stress begins to appear, which leads to a significant increase in the amplitude of the armature stress. The maximum stresses of the armature are 14.743, 35.514, 52.697, and 115.12 MPa of the four different curve radii in descending order. The common point is that stress concentration occurs in the upper tail of the armature compression side. Fig. 5(c) shows the distribution law of the high-stress area along the length of the upper rail under different curve radii of the rail. This stress is similar to the pulsation law of dynamic armature that the static rail also presents the same periodic pulsation distribution, resulting in a significant increase in the median and interval of pulsation when the curve radius decreases. Fig. 5(d) also shows that the high-stress region of the lower rail presents the same periodic distribution along the length. There is a significant increase in the distribution interval and little change in the median distribution when the curve radius decreases. Due to the asymmetry of sliding friction, the motion direction of the armature is not the same as the tangential direction of the curved rail, resulting in a slight angle difference, which leads to the tendency of the contact area of the overpressure side moving forward and the loss pressure side moving backward. Therefore, the median contact pressure of the loss side changes little but there are periodic fluctuations. The key danger lies in this pressure fluctuation. As the curve radius decreases, the amplitude of pressure fluctuation increases, resulting in a continuous decrease in the minimum contact stress. When the bending radius is 10 m, the lowest value of the maximum contact pressure is less than 3.5 MPa. In contrast, the average contact stress is only 0.15 MPa, which will lead to the deterioration of the armature–rail contact state and even transition or ablation of the rail. Fig. 5 summarizes that the curve radius of the rail will affect the armature speed and cause periodic pulsation of the stress in the armature and rail, and will lead to the imbalance of the armature–rail contact pressure with the decrease of the radius, resulting in the increase of overpressure side and the fluctuation of loss pressure side, the potentially dangerous transition or ablation of rail, and so on.

In Figs. 6 and 7, the influence of the initial armature velocity [Fig. 6(a)] and density [Fig. 7(a)] on the armature–rail contact pressure is calculated. The maximum stress along the displacement of armature [Figs. 6(b) and 7(b)], the upper and
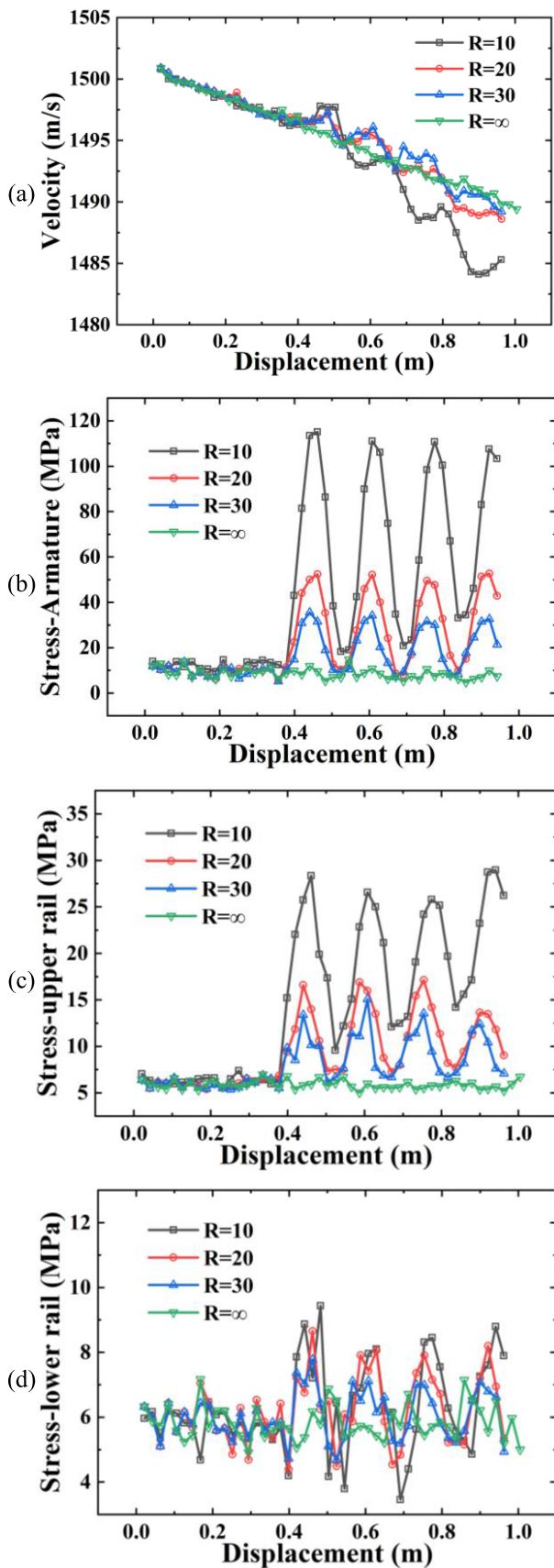
Fig. 5.   Different launching characteristic parameters vary with the armature displacement under different curve radii of rail. (a) Velocity of armature. (b) Maximum stress of armature. (c) Maximum stress of the upper rail. (d) Maximum stress of the lower rail.
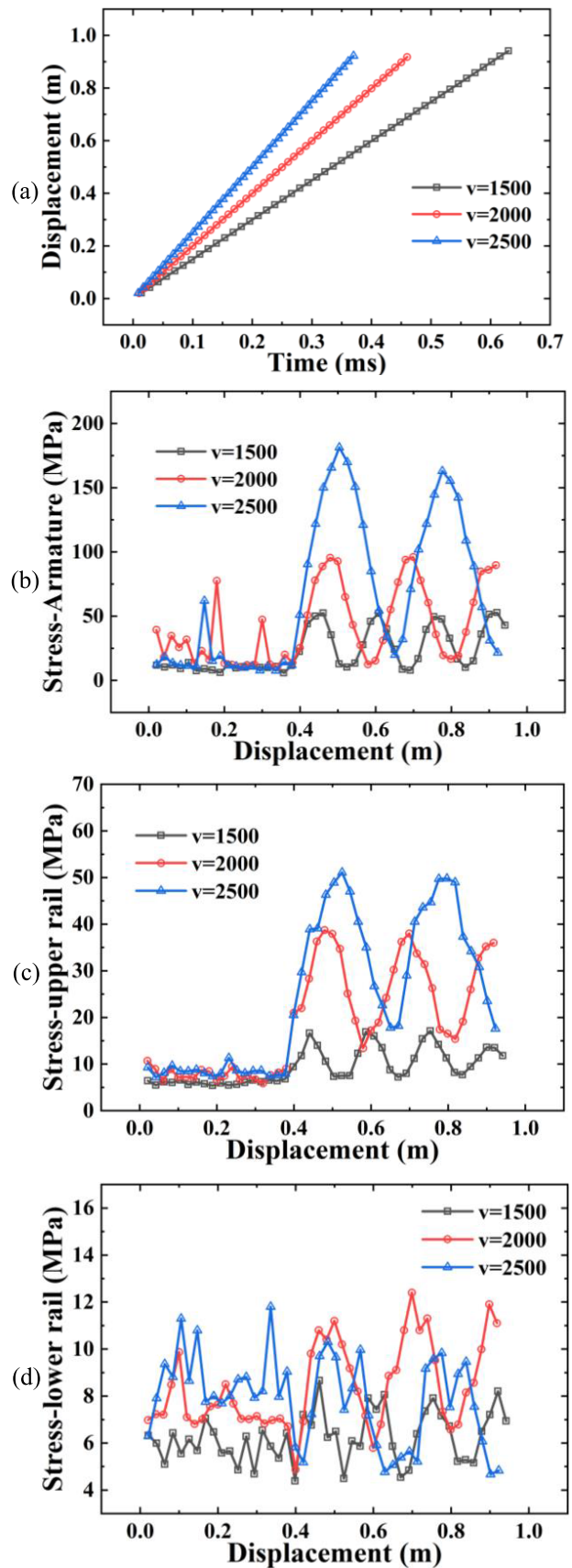
Fig. 6.   Different launching characteristic parameters vary with the armature displacement under different initial velocities of armature. (a) Timing of the launch process. (b) Maximum stress of armature. (c) Maximum stress of the upper rail. (d) Maximum stress of the lower rail.
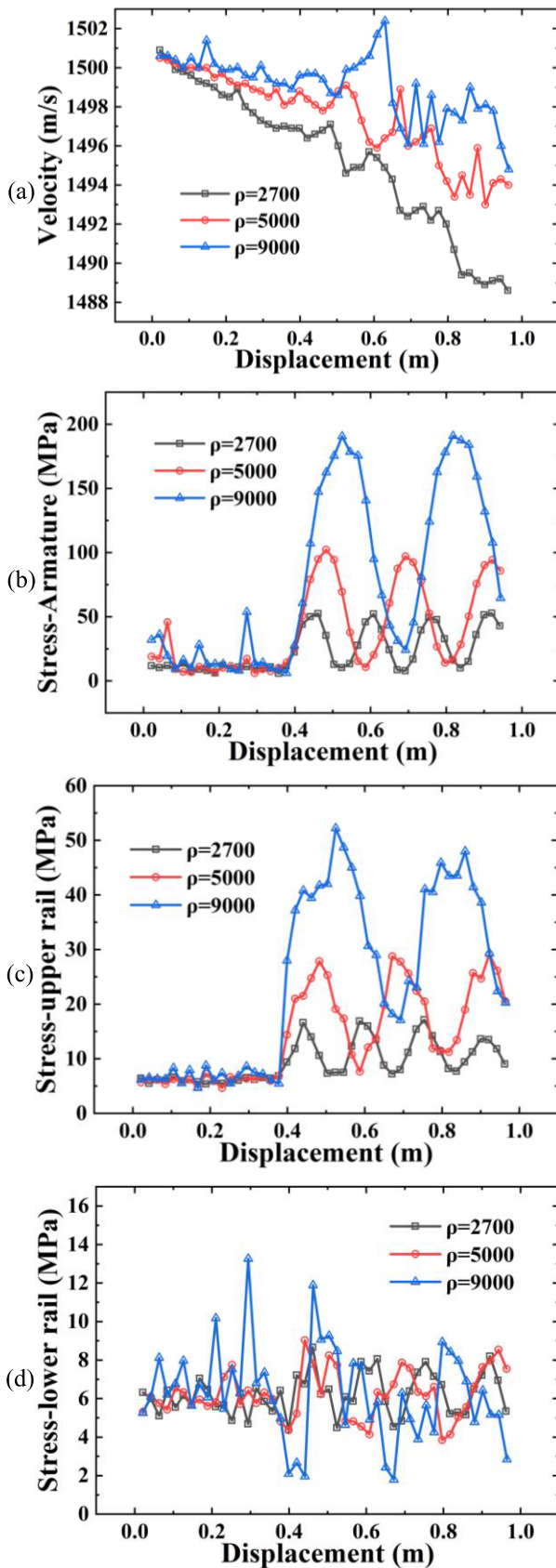
Fig. 7. Different launching characteristic parameters vary with the armature displacement under different densities of armature. (a) Velocity of armature. (b) Maximum stress of armature. (c) Maximum stress of the upper rail. (d) Maximum stress of the lower rail.

lower rail [Fig. 6(c-d)], Fig. 7(c-d) is extracted using the same analysis method of curve radius. The variation trend

and distribution law of stress are similar to the results of the curve radius. The main difference lies in the nonsame periodic pulsation distribution of the initial velocity and density of armature on the armature–rail contact stress. As the initial velocity and density of the armature increase, the cycle displacement increases accordingly. It is concluded that the armature density has an inverse correlation with the curve radius. With the increase of armature density from 2700 to 5000 to 9000 at the initial armature velocity of 1500 m/s, both the long straight and curve sections show significant velocity fluctuation and drop; besides the velocity decrease of curved sections is more obvious. The outlet velocities are 1487.4, 1492.7, and 1493.7 m/s for three different armature densities in ascending order. Their kinetic energy loss is 105.2, 113.1, and 175.7 J. Because of the increasing armature density, the mass of the armature increases, the inertia force of the armature increases, the armature–rail sliding friction increases, and the energy loss increases. In addition, compared with the initial velocity of the armature, the increased density is more dangerous because it will reduce the minimum contact pressure. When the density is 9000 kg/m^3, the minimum stress is less than 2 MPa, which is significantly lower than the initial safety value of 5 MPa. It is difficult to ensure the stability of the armature–rail contact state. Figs. 6 and 7 conclude that the distribution law of armature–rail contact pressure under different initial velocities and densities eigenvalues is relatively consistent because the selection of these eigenvalues is based on the principle that centrifugal force is positively correlated with velocity square and armature mass in (3). More importantly, when the curve radius of the rail is 20 m, the effect of centrifugal force on the armature–rail contact pressure has been dominant in this article's model.

V. CONCLUSION

In this article, the armature–rail sliding contact theoretically is derived and analyzed by finite-element simulation for the common gravity curve rail characteristics in the nonideal contact interface of electromagnetic rail launch. An armature–rail contact mechanical model with the main influencing parameters such as the curve radius was established by introducing the centrifugal force effect and equivalent electromagnetic force. The importance of the centrifugal force effect was analyzed using the 3-D finite-element simulation method, and the periodic characteristics and distribution rules of the pressure pulsation under different vertical curve radii, velocities, and densities of armature were obtained. The main conclusions are as follows.

1) The effect of centrifugal force is significant, which cannot be ignored at the interface of the curved rail, and may even play a dominant role in the armature–rail contact pressure.

2) With the decrease of the vertical curve radius and the increase of the armature density, the amplitude fluctuation of the armature–rail contact pressure on the loss pressure side becomes larger and the minimum pressure decrease, which directly leads to the deterioration of the contact state that prone to transition or ablation of rail.

REFERENCES

[1] L. Chen, J. He, S. Xia, Z. Xiao, and D. Feng, "Study on the tail structure of a C-type armature in the nonequal-cross-section cantilever model," *IEEE Trans. Plasma Sci.*, vol. 41, no. 5, pp. 1498–1502, May 2013.

[2] D. Feng et al., "Investigations of the armature–rail contact pressure distribution in a railgun," *IEEE Trans. Plasma Sci.*, vol. 43, no. 5, pp. 1657–1662, May 2015.

[3] A. P. Noel and D. P. Bauer, "Laminated barrel axial stiffness assessment [of railguns]," *IEEE Trans. Magn.*, vol. 37, no. 1, pp. 454–456, Jan. 2001.

[4] M. Werst, J. R. Kitzmiller, C. S. Hearn, and G. A. Wedeking, "Ultra-stiff, low mass, electromagnetic gun design," *IEEE Trans. Magn.*, vol. 41, no. 1, pp. 262–265, Jan. 2005.

[5] J. Nie, M. Ren, X. Kang, Q. Jiao, and J. Li, "Study on mechanical character of armature and rail with non-rectangular cross section in EML," in *Proc. 16th Int. Symp. Electromagn. Launch Technol.*, May 2012, pp. 1–5.

[6] Y. Che, W. Yuan, W. Xu, W. Cheng, Y. Zhao, and P. Yan, "The influence of different constraints and pretightening force on vibration and stiffness in railgun," *IEEE Trans. Plasma Sci.*, vol. 45, no. 7, pp. 1154–1160, Jul. 2017.

[7] W. Cheng, W. Yuan, Y. Zhao, and P. Yan, "Effects of armature characteristics on armature–rail contact performance," *IEEE Trans. Plasma Sci.*, vol. 45, no. 7, pp. 1380–1386, Jul. 2017.

[8] W. Xu et al., "Velocity precision analysis with the small caliber electromagnetic launch," *IEEE Trans. Plasma Sci.*, vol. 45, no. 7, pp. 1394–1398, Jul. 2017.

[9] W. Zhao, W. Tian, W. Yuan, and P. Yan, "Armature ejecta and its effects on insulator degradation in solid-armature launchers," *IEEE Trans. Plasma Sci.*, vol. 50, no. 2, pp. 489–495, Feb. 2022.

[10] Z. G. Tian et al., "Dynamic response of composite rail during launch process of electromagnetic railgun," *Acta Armamentarii*, vol. 38, no. 4, pp. 651–657, 2017.

[11] P. Pei, B. Cao, X. Ge, and M. Li, "Analysis of the influence of bore spacing variation on the electromagnetic launching process," in *Proc. 16th Annu. Conf. China Electrotech. Soc.*, vol. 899, 2022, pp. 1430–1439.

[12] J. Lu and W. Ma, *Electromagnetic Rail Launch Theory and Technology*. Beijing, China: Science Press, 2020, pp. 9–11.

[13] B. Li, J. Lu, S. Tan, Y. Jiang, and Y. Zhang, "Effect of interfacial roughness of sliding electrical contact on the melting characteristics of armature," *Trans. China Electrotech. Soc.*, vol. 33, no. 7, pp. 1607–1615, 2018.

[14] S. Moaveni, *Finite Element Analysis Theory and Application With ANSYS*. Beijing, China: House of Electronics Industry, Jan. 2008.

Yunlong Che was born in Beijing, China, in 1989. He received the master's degree from the School of Energy and Power Engineering, Beihang University, Beijing, in 2014.

Since 2014, he has been with the Institute of Electrical Engineering, Chinese Academy of Sciences, Beijing. His current research interests include structural strength, vibration, and applications of large current pulse discharge.

Weiqun Yuan was born in Danyang, Jiangsu, China, in 1976. He received the Ph.D. degree from the Department of Kinetic Engineering, Nanjing University of Science and Technology, Nanjing, China, in 2003.

He is currently with the Institute of Electrical Engineering, Chinese Academy of Sciences, Beijing, China, where he has been involved in high-voltage pulse discharge and its applications.

Wu Yuan was born in Handan, Hebei, China, in 1984. He received the Ph.D. degree from the Institute of Mechanics, Chinese Academy of Sciences, Beijing, China, in 2015.

He is currently with the Institute of Mechanics, Chinese Academy of Sciences, Beijing. His current research interests include lightweight structures, cellular materials, and laser–matter interactions.

Zhizeng Wang, photograph and biography not available at the time of publication.

Wei Hao, photograph and biography not available at the time of publication.

Ying Zhao, photograph and biography not available at the time of publication.

Ping Yan, photograph and biography not available at the time of publication.